communications earth & environment

ARTICLE

https://doi.org/10.1038/s43247-021-00170-2 OPEN

Biosignatures of ancient microbial life are present across the igneous crust of the Fennoscandian shield

Henrik Drake [1✉], Nick M. W. Roberts[2], Manuel Reinhardt [1], Martin Whitehouse [3], Magnus Ivarsson[3], Andreas Karlsson [3], Ellen Kooijman[3] & Melanie Kielman-Schmitt[3]

Earth's crust contains a substantial proportion of global biomass, hosting microbial life up to several kilometers depth. Yet, knowledge of the evolution and extent of life in this environment remains elusive and patchy. Here we present isotopic, molecular and morphological signatures for deep ancient life in vein mineral specimens from mines distributed across the Precambrian Fennoscandian shield. Stable carbon isotopic signatures of calcite indicate microbial methanogenesis. In addition, sulfur isotope variability in pyrite, supported by stable carbon isotopic signatures of methyl-branched fatty acids, suggest subsequent bacterial sulfate reduction. Carbonate geochronology constrains the timing of these processes to the Cenozoic. We suggest that signatures of an ancient deep biosphere and long-term microbial activity are present throughout this shield. We suggest that microbes may have been active in the continental igneous crust over geological timescales, and that subsurface investigations may be valuable in the search for extra-terrestrial life.

[1] Department of Biology and Environmental Science, Linnæus University, Kalmar, Sweden. [2] Geochronology and Tracers Facility, British Geological Survey, Nottingham, UK. [3] Swedish Museum of Natural History, Stockholm, Sweden. ✉email: henrik.drake@lnu.se

The deep biosphere realm includes sediments and both sedimentary and igneous-rock environments[1,2], and is estimated to represent one-tenth to one-third of all live biomass[3,4]. Considering the vastness of this biosphere, it is reasonable to assume that the microbial processes strongly affect the energy cycles of our planet, including production and consumption of greenhouse gases[5], but the extent is not yet known. Although the understanding of deep biosphere metabolisms has evolved over the recent years, the observations are still patchy. For the continental crust, this scarcity is generally owing to the small number of deep boreholes, underground observatories, and mines that allow and enable research dedicated to the deep biosphere.

Precambrian crystalline rock makes up the largest volumes of the continental crust, accounting for >70% of the total continental surface area and >80% of crust at depths below 2 km[6,7]. Environmental conditions in this cryptic habitat shift rapidly to anoxic within the upper tens of meters[8]. The majority of microorganisms living in deep fracture water therefore maintain an anaerobic lifestyle in the absence of sunlight and scarcity of organic carbon sources[9]. Metabolic pathways include sulfate reduction, fermentation, acetogenesis, methanogenesis, and methanotrophy[10–14].

The deep biosphere is believed to host some of the most ancient evolutionary lineages[2,15] and has been proposed to have held the majority of Earth's live biomass prior to plant colonization of land ~400 Ma ago[16]. This suggests that deep environments, including ocean floors, have dominated on Earth for most of life's history. However, in similarity with live communities, knowledge of the extent and nature of ancient microbial activity in the deep continental crust is still scarce. Studies that address deep ancient life in the igneous continental crust by combining either isotopic, morphological, or molecular biosignatures with geochronology only exist from a few Fennoscandian shield sites (Fig. 1, yellow symbols). These studies revealed deep microbial activity dating back to the Devonian, marked by isotopic signatures of vein minerals, as well as morphological support for ancient microbial activity[17–23]. Morphological reports of putative prokaryotes and/or eukaryotes exist from basalt vesicles in South Africa[24], USA[25], Japan[26], and mines in Germany[27]. From the oceanic igneous crust, examples include fossilized fungal communities at seamounts in the Pacific and Atlantic oceans[28,29], and molecular biosignatures in carbonates of the Lost City hydrothermal field at the Iberia margin[30]. In the Fennoscandian shield, the morphological evidence of ancient subsurface microbial life include chitin-bearing partly preserved and partly mineralized fungal hyphae[31], and putative prokaryotic cells preserved within calcite veins[17]. It still remains unclear whether the biosignatures from the few sites described so far are anomalous or represent the bulk of the habitable continental igneous crust over geological timescales.

Here we assess how widespread biosignatures of deep ancient life are in the continental igneous crust of the Fennoscandian shield by analyzing low-temperature mineral specimens containing euhedral calcite and pyrite in fractures and cavities, frequently in spatial relation to solid bitumen (altered crude oil, e.g., through devolatilization or biodegradation, ref. [32] and references therein), collected from 33 abandoned mines (as deep as 1400 m) in Paleoproterozoic rocks across the shield, dominantly in the Swedish part (Fig. 1, close up of the most frequently sampled Bergslagen area in Supplementary Fig. 1). A multi-method approach is applied, involving high spatial resolution analytical transects for both U-Pb geochronology and stable isotopes of carbon, oxygen, strontium, and sulfur across mineral grains. Additional isotope determinations are made on the bulk sample scale and within single crystals via ion imaging. The molecular composition of solid bitumen and biomarkers from the mineral coatings are determined, including the stable carbon isotope composition of specific organic compounds.

We show that biosignatures of ancient microbial life are omnipresent in the shield, confirming that previous scattered observations are not anomalous. Our multi-proxy study confirms that ancient microbial methanogenesis and sulfate reduction have been ubiquitous over geological time and temporal shifts between these dominating microbial metabolisms are determined. The documented preservation of biosignatures in mineral veins over geological timescales and establishment of the timing of these microbial processes sheds light not only on the evolution and extension of deep life over time on Earth but also has important implications for astrobiological exploration strategies[33].

Results

Carbonate carbon system. Euhedral calcite in the cavities and veins occurs in several generations as shown by zonation detected in crystal cross-sections (Fig. 2b, f) and secondary ion mass spectrometry (SIMS) analytical transects (Fig. 2c, g, summary in Supplementary Data 1, full data in Supplementary Data 2–4). In samples from Kallmora and Grängesberg, the zonation is particularly well established. The oldest calcite phase is of blocky habit and is intergrown with bitumen, and is thus related to bitumen emplacement in the fracture system (Figs. 2a and 3a, b). This calcite generation has relatively low $\delta^{18}O$ values (−18 to −11‰$_{V\text{-}PDB}$) and $\delta^{13}C$ values of 0 ± 2‰. At Kallmora, the first phase after the bitumen precipitation is euhedral calcite with heavy $\delta^{13}C$ values (+5.5 to +10.2‰, Overgrowth I, OGI) and with $\delta^{18}O$ values of around −4 ± 0.5‰. In Kallmora sample #18910193, this generation occupies the whole crystals (Fig. 2c), whereas in Kallmora #19334861 and #18910078, this phase is followed by several overgrowths: OGII: with positive $\delta^{13}C$ (+1.2 to +10.2‰, Figs. 2g and 3e) and lighter $\delta^{18}O$ (−8.4 to −7.3‰, similar for following generations); OGIII: a thin zone with moderately negative $\delta^{13}C$ values (−7.9 to −3.7‰) followed by microcrystalline porous calcite overgrowths IV and V, with more negative $\delta^{13}C$ values (−15.8 to −12.3‰). Aggregates of euhedral, cubic to tabular pyrite, are intergrown with the calcite OGIV–OGV, which partly to completely covers the pyrite aggregates (Fig. 3c). At Grängesberg (Supplementary Fig. 2) and Riddarhyttan, similar trends as that at Kallmora of ^{13}C-rich calcite ($\delta^{13}C$ values up to +27‰) being succeeded by porous ^{13}C-poor calcite (down to −27‰) occur (Supplementary Fig. 2). Homogeneous ^{13}C-rich calcite occurs at Nyäng. At Storstreck, Garpenberg, and Dannemora mines, and Karlevi quarry, ^{13}C-rich calcite growth zones are common. In total, 15 samples from 10 mines carried ^{13}C-rich calcite ($\delta^{13}C$: +3 to +27‰) down to depths of ~800 m and 9 additional mines featured significantly ^{13}C-depleted calcite ($\delta^{13}C$: −29 to −17‰).

Carbonate geochronology. The growth zonation of the Kallmora samples described above was targeted for high spatial resolution U-Pb geochronology using laser ablation inductively coupled MS (LA-ICP-MS), in the same crystals that were targeted for SIMS microanalysis for C and O isotopes. OGI yielded an age of 51.1 ± 2.3 Ma (Fig. 2d and Supplementary Data 5 and 6) in sample #18910193, where it makes up the whole crystals. Sample #18910078 also features OGI, but although the two spots yielded ages broadly overlapping with #18910193 (58 ± 11 Ma), they do not provide a robust age estimate (Fig. 2h). Growth zone OGII was targeted in #18910078 and #19334681, and yielded overlapping ages of 34.9 ± 2.0 Ma and 30.0 ± 6.6 Ma, respectively (Figs. 2h and 3f, g). Growth zone OGIII was too thin for a single age determination, but spots that overlap this zone in #18910078 and #19334681 are ca. 23 Ma and ca. 26 Ma, respectively, confirming persistent younging trends of each growth zone across these samples. Twenty-three spots for OGIV–OGV yielded ages

Fig. 1 Map of the Fennoscandian shield showing the study sites for deep ancient biosignatures. Previously studied sites (Lockne[18,19], Siljan[21], Forsmark[22,23,34], Laxemar[17,20,66,73]) are marked by yellow symbols. Magenta symbols mark samples with isotopic, molecular, and/or morphological biosignatures, whereas turquoise blue symbols mark mineral samples with no distinctive biosignatures. The base map is used with permission, © Geological Survey of Sweden.

ranging from 18.9 to 14.3 Ma for #19334681, with no discernible sub-populations; the data imply that the growth zoning is higher resolution than the laser sampling spot (Fig. 3g and Supplementary Fig. 3). For #18910078, a similar age span is present for OGIV–OGV (21.2 to 13.6 Ma), but two groups with intercepts at 15 ± 2.9 and 13.7 ± 0.6 Ma are more clearly discernible for the main crystallization phases for this sample (Fig. 2h).

A complementary relative timing indicator is the ^{87}Sr over ^{86}Sr ratio. LA-multi collector (MC)-ICP-MS transects for Sr isotopes were made in corresponding spots as for C and O in the calcite crystals. The Kallmora sample #18920193 shows similar and overlapping values in the range 0.7262 ± 0.0013 ($n = 4$), suggesting formation at a single event. The #18910078 sample that features several overgrowths and the OGI has overlapping $^{87}Sr/^{86}Sr$ (0.7247 ± 0.0026) with the corresponding growth zone in #18920193. The later zones have overlapping values (OGII-OGIII: 0.7257 ± 0.0028, $n = 6$), although generally turning into lower values in the outermost growth zones (OGIV–OGV, 0.7183–0.7249). A Nygruvan, Norberg sample (#19090180), shows C and O, and $^{87}Sr/^{86}Sr$ composition in agreement with OGI of the Kallmora samples (0.72759 ± 0.00070). Calcite with heavy $\delta^{13}C$ values in several mines have $^{87}Sr/^{86}Sr$ in the same range (Riddarhyttan, Grängesberg/Grängesberg-Malingsbo, $n = 6$, 0.72787 ± 0.00065) as Kallmora and Nygruvan in Norberg.

Sulfur system. Pyrite was analyzed for $\delta^{34}S$ in 25 samples from 19 mines and had highly variable values, with an overall range between −39 and +147‰. The largest range in an individual sample and also within a single crystal was 127‰. Superheavy pyrite $\delta^{34}S$ values were detected at several sites, e.g., Kallmora (up to +147‰), Grängesberg (+98‰), Gräsberg (+86‰), Ställberg (+81‰), and Storstreck (+50‰). Transects of SIMS microanalyses dominantly show a trend from lighter values in the interior and successively heavier in the outer growth zones. A noteworthy feature is that samples with superheavy pyrite do not contain any extremely depleted values (lightest part being in the range −13 to +38‰). The isotopically most diverse pyrite was from Kallmora and shows evolution of $\delta^{34}S$ from around +20–50‰ in the crystal interior towards heavier values with growth up to the maximum detected values of around +147‰. SIMS ion images show that the $\delta^{34}S$ increase is not steady and straightforward. Instead, the $\delta^{34}S$ shows dips and spikes that are petrographically related to growth zones (Fig. 4 and Supplementary Fig. 4). The crystals are terminated by a zone of lighter pyrite that approaches similar values as the core (~+30–50‰). Bulk sample values for these Kallmora samples were +81.4 ± 1.1‰ and +81.3 ± 1.0‰.

Organic signatures from calcites and bitumen. Calcite from Kallmora (#18920193 and #19334861) and Stråssa (#19210370) was analyzed for trapped organic molecules (via gas chromatography–mass spectrometry; GC-MS). Calcite dissolution released robust above blank concentrations of unsaturated regular ($C_{16:0}$–$C_{24:0}$) and methyl-branched (*i*-$C_{17:0}$, *ai*-$C_{17:0}$, and *i*-$C_{18:0}$) fatty acids, as well as monounsaturated regular fatty acids

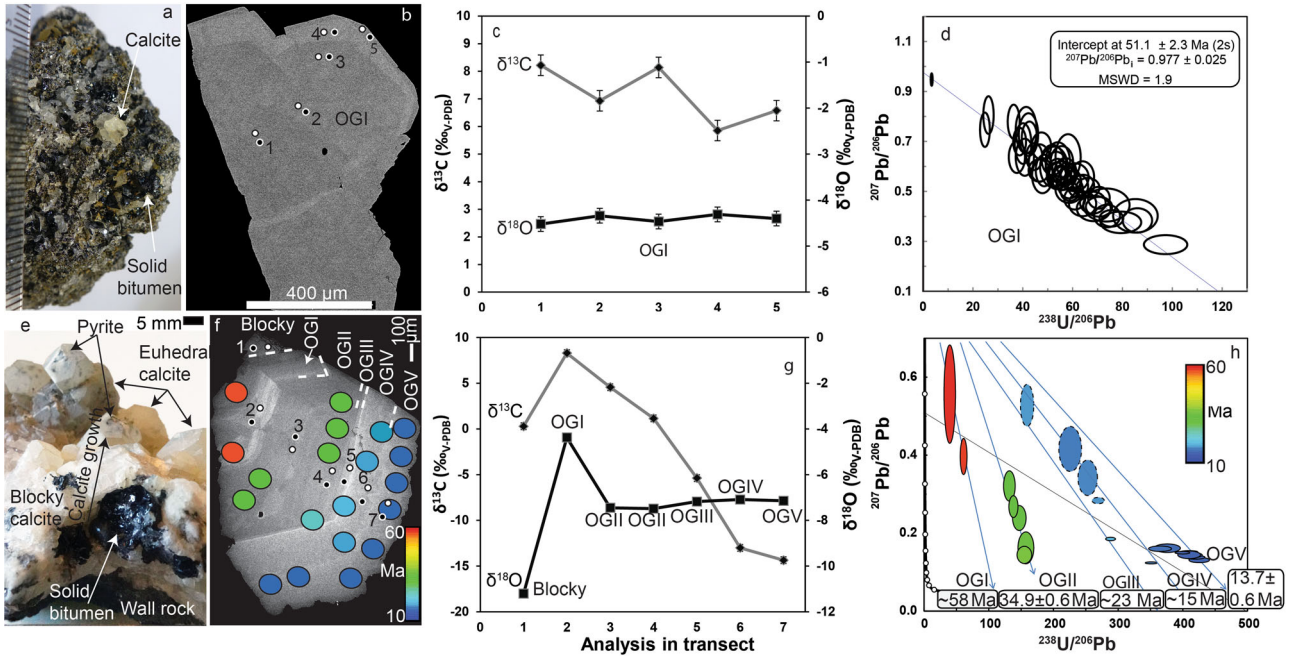

Fig. 2 Microscale isotope and geochronology determinations. Two samples from Kallmora are shown (#18920193 (**a**–**d**) and #18910078 (**e**–**h**)). **a**, **e** Photographs of the fracture samples, in both cases precipitation has started from the fracture wall with a blocky calcite in paragenesis with bitumen followed by younger calcite overgrowths with pyrite (**e**). **b**, **f** Polished calcite crystal cross-section of hand-picked crystals from **a**, **e** with different crystal overgrowth (OG) zones indicated, as well as spot locations for SIMS and LA-ICP-MS. **c**, **g** SIMS transects of C and O isotopes corresponding to the spot locations in **b**, **f**. **d**, **h** Tera-Wasserburg plots showing U-Pb age groups from LA-ICP-MS spots; for **h**, different colors denote different age groups and the symbols with stippled line are from other crystals than (**f**). Age plot for all OGIV–OGV spots in **h** is in Supplementary Fig. 3. Photograph (**a**) includes mm-marked ruler for scale. Error bars/ellipses (1σ for SIMS and 2σ for LA-ICP-MS) are shown, or are within the size of the symbols.

($C_{18:1}$, Fig. 5). Only a few other compounds were detected, but could not be identified due to low abundance and/or coelution (i.e., stayed in the fatty acid methyl ester fraction after column chromatography; see "Methods" section). $C_{16:0}$ and $C_{18:0}$ were most abundant in all calcite samples, with highest amounts in the Kallmora samples (ca. 4 p.p.m.; Supplementary Data 7, Supplementary Fig. 6). Kallmora #19334861 shows the highest concentrations of methyl-branched fatty acids. GC–combustion–isotope ratio MS (GC-C-IRMS) analysis of its purified fatty acid fraction revealed $\delta^{13}C$ values of −29.3 ± 0.2‰ for $C_{16:0}$, −41.0 ± 3.5‰ for *ai*-$C_{17:0}$, −38.6 ± 3.8‰ for $C_{17:0}$, and −29.7 ± 0.3‰ for $C_{18:0}$ (Fig. 5). The $\delta^{13}C$ values of $C_{20:0}$, $C_{22:0}$, and $C_{24:0}$ could not be determined due to coelutions or low abundance.

Solid bitumen from Kallmora was analyzed with GC-MS (maltene fraction) and elemental analysis. The maltene fraction only contained an unresolved complex mixture (UCM, Supplementary Fig. 5), which could not be characterized further. The solid bitumen has a bulk $\delta^{13}C$ of −30‰ and a carbon content of 79 wt%.

Morphology. Complex microbial morphologies occur in samples from six sites, at variable degree of preservation. In the sample from Lund (#19360094), an interconnected network of filamentous structures are observed in relation to bitumen (Fig. 6a, c–e). The filaments are between 10 and 20 µm in diameter and over 100 µm in length. They branch frequently and anastomoses between branches occur. The transition from a biofilm to an interconnected network suggests that the film represent a biofilm from which the filaments protrude. The filaments are almost completely mineralized by clays with calcite and pyrite, which indicate the filaments are indigenous and not modern contaminants. In a few other samples from, e.g., Dannemora (#g22202), mineralized or partly mineralized filaments are observed. They are usually associated with, and protrude from, a carbonaceous film on the mineral surfaces. However, a lack of diagnostic and complex morphology makes interpretation and conclusions on biological affinity scarce. In sample #19920262 from Grängesberg, >1 mm-long curvi-linear filaments with a dimeter of ~10 µm are associated with globular bitumen (Fig. 6g, h). The filaments grow from a biofilm at a pyrite crystal surface and micro-crystalline pyrite occur on their surface. The filaments are partly carbonaceous with a similar but slightly higher back-scatter intensity compared to the bitumen spheres, but no diagnostic morphology can be observed. At Riddarhyttan (#20180313), the bitumen film has longitudinal corrosion features (Fig. 6b, f). They occur either as randomly, or irregularly distributed, longitudinal textures of similar ~10 µm diameters.

Discussion

Isotopic evidence for deep ancient life across the Fennoscandian Shield. Isotope records of carbon in calcite ($\delta^{13}C$: −29 to +27‰) and sulfur in pyrite ($\delta^{34}S$ −39 and +147‰) show a substantial variability that suggests microbial influence in a majority of the mines (Supplementary Data 1). The Kallmora samples, in similarity with most of the studied sites, show an initial precipitation of solid bitumen and calcite. This site is used as the main example for detailed isotopic interpretations. The oldest blocky calcite type has relatively low $\delta^{18}O$ values (Fig. 2g) but no C isotope signature specific for methanogenesis or methane oxidation, in agreement with previous findings of blocky bitumen-related calcite at Forsmark, Sweden (Fig. 1)[23]. At Forsmark and also at Laxemar, the calcite of this type has fluid inclusion compositions that support formation from a 80–95 °C brine fluid and Rb-Sr geochronology of coeval calcite-K-feldspar indicates Devonian–Carboniferous precipitation[22,23,34]. This suggests that bitumen infiltrated the deep igneous-rock fracture

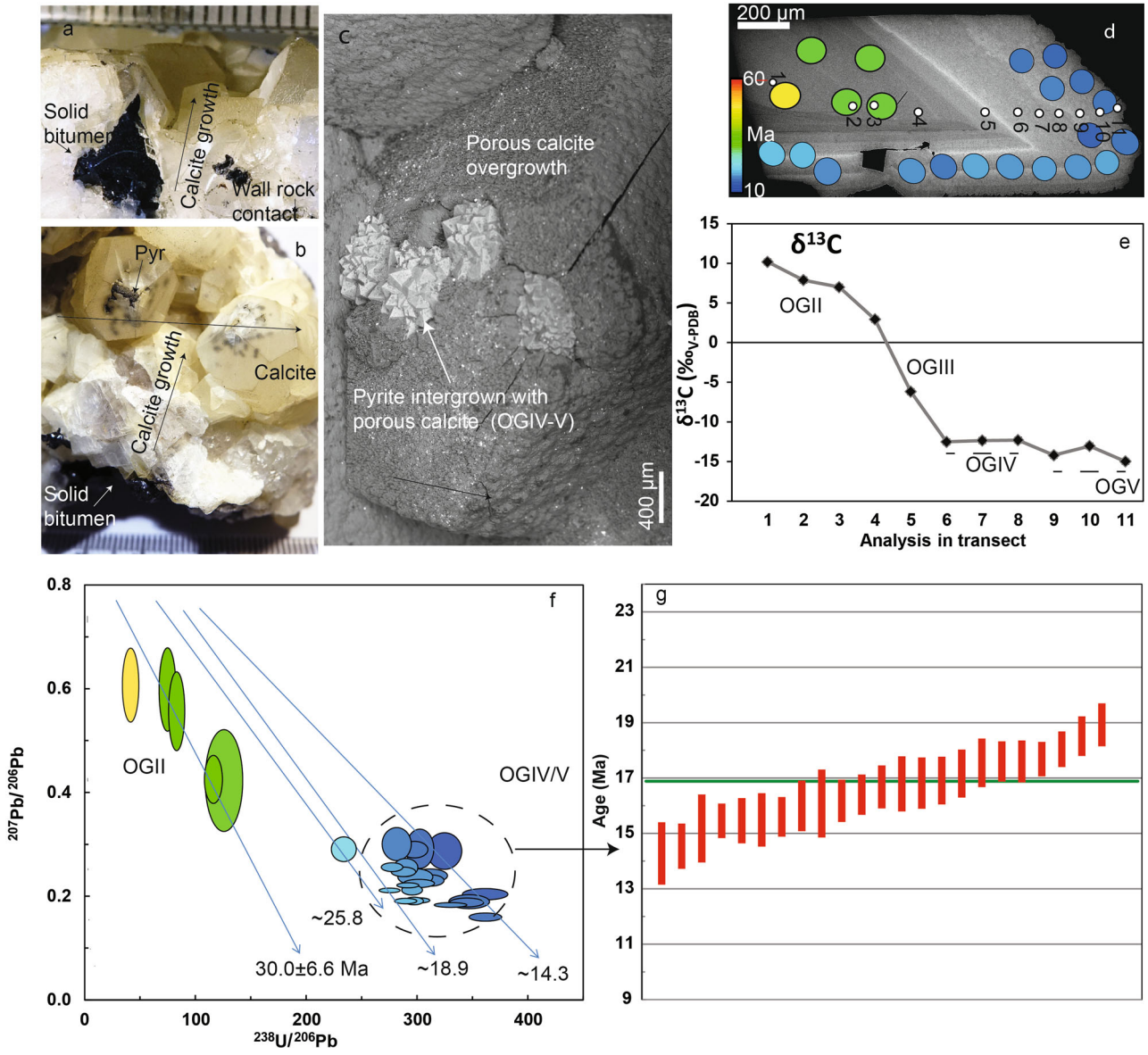

Fig. 3 Microscale isotope and geochronology determinations. One sample from Kallmora is shown (#19334861). **a**, **b** Photographs of the fracture samples; in both cases, precipitation has started from the fracture wall with a blocky calcite in paragenesis with bitumen followed by younger calcite overgrowths with pyrite, as also seen in the back-scattered SEM image (**c**). **d** Polished calcite crystal cross-section of hand-picked crystals from **a**–**c** with different crystal overgrowth (OG) zones indicated, as well as spot locations for SIMS and LA-ICP-MS. **e** SIMS transects of C and O isotopes corresponding to the spot locations in **d**. **f** Tera-Wasserburg plot of U-Pb age groups from LA-ICP-MS spots; for **d**, different colors denote different age groups and the ages of OGIV/V are plotted separately in **g** (a few spots on growth zone boundaries were rejected after quality control, see Supplementary Data 6). Error bars/ellipses (1σ for SIMSLA-ICP-MS and 2σ for LA-ICP-MS) are shown, or are within the size of the symbols.

networks at tectonic events when temperatures where elevated in the sedimentary rock pile due to thickening of a Caledonian foreland basin[35]. These elevated temperatures caused bitumen expulsion from organic-rich black shales of various types (e.g., lower Cambrian alum shale[36,37] and Silurian Fjäcka shale[38]). The bitumen at Kallmora (Fig. 2) and at other study sites suggest that bitumen expulsion from overlying (but presently largely eroded) sedimentary rocks was ubiquitous in the deep igneous-rock fracture network of the Fennoscandian shield during post Caledonian foreland basin development. We focus the following discussion on biosignatures in mineral assemblages that succeed the bitumen emplacement, in particular to calcite overgrowths that show highly variable $\delta^{13}C$ values between different growth zones, pointing toward shifts in microbial metabolisms.

Isotopic evidence for microbial methanogenesis. The first stage of euhedral calcite overgrowths has $\delta^{13}C_{calcite}$ of up to +10.2‰ at Kallmora (Fig. 2c, g) and up to +27‰ elsewhere. ^{13}C-rich residual CO_2 is a commonly used diagnostic marker for the formation of secondary methane from biodegradation of seep oils and petroleum[39,40], owing to the discrimination that occurs against ^{13}C during methanogenesis. The significant ^{13}C-enrichment observed in OG1–2 calcite at Kallmora is therefore proposed to reflect calcite formation following secondary microbial methane formation in situ. Microbial methanogenesis is commonly linked to sulfate-poor biodegraded petroleum reservoirs[41]. It may involve initial biodegradation steps of fermentation of the expelled hydrocarbons (bitumen/seep oil) leading to the formation of, e.g., acetic acid, H_2 and CO_2[42], which can fuel

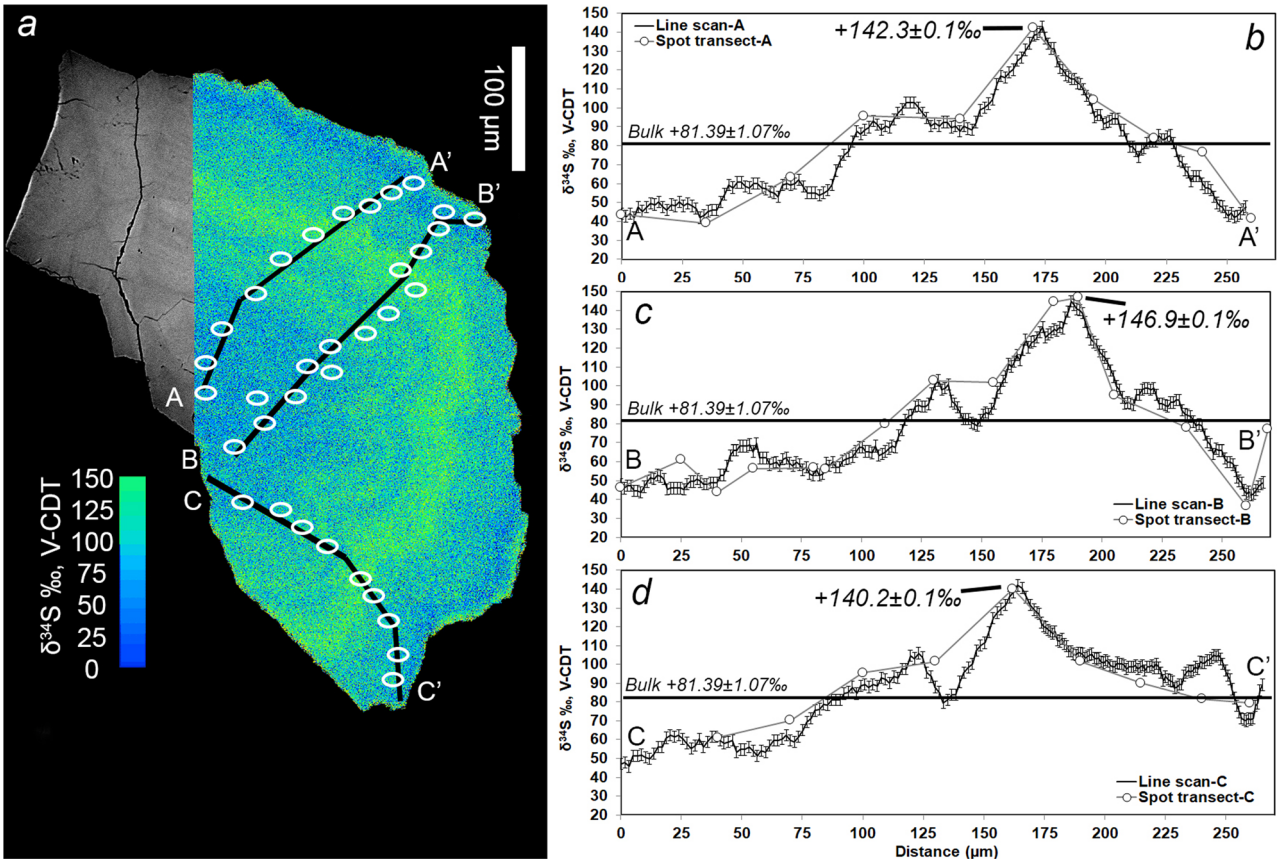

Fig. 4 Sulfur isotope variability in pyrite. a SEM image of a polished pyrite crystal from Kallmora (#19334861), draped by a composite of eight SIMS ion imaging renderings, with three ion imaging line scans (A-A′, B-B′, C-C′) and corresponding analytical transects of 10 µm SIMS spots for $\delta^{34}S$. The color coding of the ion images is normalized and anchored to the SIMS spots. **b**–**d** Transects of SIMS spots together with $\delta^{34}S$ values from corresponding line scans in the ion images and bulk $\delta^{34}S$ of the sample. Pyrite mineral identification is confirmed by X-ray diffraction (Supplementary Fig. 7). Error bars are indicated (1σ).

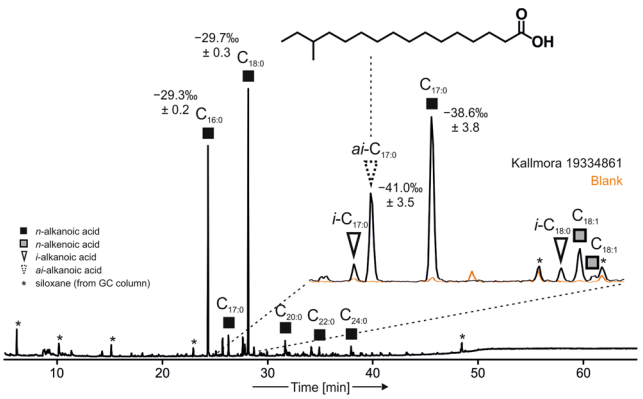

Fig. 5 Gas chromatogram of calcite-trapped molecules. The chromatogram (total ion current) shows fatty acids that were trapped in calcite from Kallmora (#19334861), including compound-specific isotope values for $C_{16:0}$, *ai*-$C_{17:0}$, $C_{17:0}$, and $C_{18:0}$. The blank is shown in orange. Note that all fatty acids were analyzed as methyl esters (see "Methods" section). The structural formula represents *anteiso*-heptadecanoic acid.

methanogenesis, but as bitumen hydrocarbons are fully saturated, an oxidant may be required, potentially in the form of sulfate reducers oxidizing the organic carbon[43]. These bitumen biodegradation pathways were proposed for formation of microbial methane and ^{13}C-rich CO_2, and authigenic calcite in deep basement fractures of the Siljan impact structure in Sweden[21]. Studies of deep granite fracture networks in the UK have also suggested that the presence of solid bitumen/seep oils may have provided an energy source for in situ microbial activity[44]. Large C isotope fractionation and, consequently, production of a ^{13}C-rich residual CO_2 is common for the CO_2 reduction methanogenesis pathway, in contrast to the acetate fermentation pathway[45], which suggests that the methanogens in the studied mines utilized the carbonate reduction pathway.

The timing of methanogenesis is assigned directly by the authigenic ^{13}C-rich calcite formation ages derived from the in situ U-Pb dating and gives a 51 ± 2 Ma age for the first ^{18}O-rich calcite stage (OGI) and a 35–30 Ma age range for the following stage (OGII) (Fig. 2). The shift in $\delta^{18}O$ of the calcite indicates that methanogens were active in fluids of two distinctly different origins, or at various temperatures, as O isotope fractionation between calcite and water is highly temperature sensitive[46]. These ages overlap with ages of methanogenesis-related calcite from Siljan[21] and to discrete, supposedly Alpine-related reactivation events of platform sediment fractures in Sweden, derived by slickenfibre U-Pb geochronology[47].

Isotopic evidence for microbial sulfate reduction. Later calcite overgrowths at Kallmora, in particular OG4–5, which feature ^{13}C-depleted signatures (−15.8‰) indicate that methanogenesis ceased to dominate in the fracture system. Instead, the ^{13}C-depleted signatures suggest organotrophy. At this stage, pyrite started to precipitate. Pyrite forming due to microbial

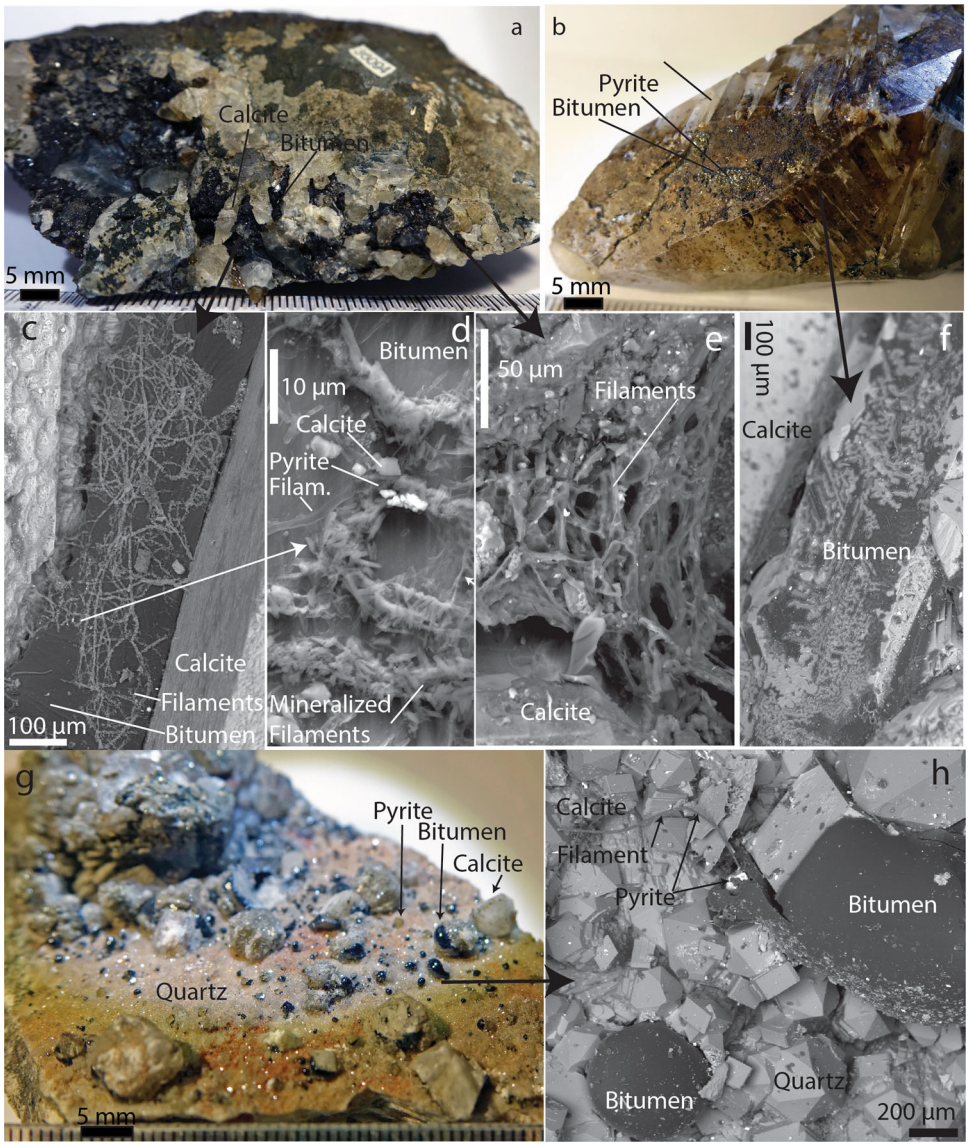

Fig. 6 Filaments and degraded bitumen. a Photograph and **c**–**e** BSE-SEM images of mineralized filaments in a mycelium-like network on bitumen, adjacent to calcite (and younger calcite exist on the filaments as well, **d**). Branching is frequent and anastomoses between branches occur occasionally (**e**). The morphology, size, and occurrence indicate a fossilized fungal mycelium. The complete mineralization and presence of pyrite (**d**) on the filaments further indicate the mycelium to be an indigenous feature and not a modern contaminant. **b** Photograph and **f** BSE-SEM image of corrosion textures in bitumen on calcite from Riddarhyttan (#201803013). **g** Photograph and **h** BSE-SEM image of a curvi-linear filament growing from a biofilm associated with pyrite and solid bitumen, on a fracture surface with an older quartz coating and calcite, from Grängesberg (#19670390). Fine-grained pyrite (BSE-bright spots at arrow) occurs on the filaments. Photographs include mm-marked ruler for scale.

sulfate reduction (MSR) inherits the S isotopic composition of the hydrogen sulfide[48]. As the MSR metabolism produces hydrogen sulfide strongly depleted in ^{34}S, $\delta^{34}S_{pyrite}$ serves as a marker for MSR, whereas heavy values commonly develop in systems undergoing Rayleigh isotope fractionation[49]. In several of the mines, the $\delta^{34}S_{pyrite}$ values are significantly depleted, down to −39‰. The initial sulfate $\delta^{34}S$ values are unknown but similar settings (Laxemar and Forsmark, Sweden) have been shown to hold $\delta^{34}S$ values in the +16–27‰ range for sulfate minerals and dissolved sulfate in the fracture systems[50]. This implies a maximum $^{34}\varepsilon$ value ($^{34}\varepsilon = \delta^{34}S_{SO4} - \delta^{34}S_{pyrite}$) of 55–66‰, in line with MSR[51,52], and rules out thermochemical sulfate reduction (TSR), which produces $^{34}\varepsilon$ of up to 22‰, but usually much less[53]. Low minimum $\delta^{34}S_{pyrite}$ values implying apparent MSR-related $^{34}\varepsilon$ values occur in 10 of 19 mines analyzed for $\delta^{34}S_{pyrite}$. The S isotope composition of the bitumen is not known, but sulfur isotope determinations of solid bitumen from other areas point to similar $\delta^{34}S$ values of this material as the anticipated initial sulfate described above, c.f. the Big Piney–La Barge oil and gas field in Wyoming (+18.9 ± 3.9‰)[54], and the Puguang and Yuanba gas fields (+12.0 to +34.2‰) of the Sichuan Basin, China[55].

For the Kallmora samples, the minimum $\delta^{34}S_{pyrite}$ values are relatively heavy, +18.4‰, and a complex evolution towards heavier values is evident (Fig. 4 and Supplementary Fig. 4). After the peak in values at +147‰, the values drop towards the rim. To achieve superheavy $\delta^{34}S_{pyrite}$ values, Rayleigh reservoir effects in semi-closed systems are generally needed[56,57]. These effects arise when MSR occurs at rates higher than the supply by advection and diffusion such that the dissolved sulfate pool shrinks, whereby the $\delta^{34}S$ increases. However, if there are large relative quantities of superheavy pyrite formed, there is an obvious mass balance problem that cannot be explained by a simple Rayleigh

fractionation cycle, as isotopically heavy pyrite would only form in the very last portion of closed system MSR[57]. In addition, if all sulfate is consumed, the mean $\delta^{34}S$ of all pyrite formed should be equal to the $\delta^{34}S$ of the initial sulfate. At Kallmora, the bulk values of aliquots of several ground pyrite crystals are at +81 ± 1‰. This means that the $\delta^{34}S$ of the sulfate was already significantly affected by MSR before reaching the investigated cavities. The relatively heavy inner part of the crystals (+18‰) is also indicative of an onset of pyrite precipitation from a ^{34}S-enriched initial sulfate, which, if a $^{34}\varepsilon$ of 55–66‰ is assigned, gives an initial $\delta^{34}S_{SO4}$ of 73–84‰, which overlaps with the bulk pyrite at +81‰. The evolution towards the heaviest value in the crystal is not straightforward, but features dips that may be due to fluid inflow and mixing events. Similarly, the decreasing $\delta^{34}S_{pyrite}$ values in the outermost overgrowths can be due to dilution of the $\delta^{34}S_{sulfate}$ pool by infiltrating fluids. Superheavy SIMS values for samples from Storstreck and Grängesberg are also associated with significantly ^{34}S-enriched bulk values (Supplementary Data 1).

Further environmental support for microbial origin for the superheavy $\delta^{34}S$ values is provided by the documented low-temperature conditions at the time. The U-Pb geochronology shows the pyrite-calcite assemblage at Kallmora formed at 19–13 Ma (Fig. 2). Thermochronological investigations of the south and central Fennoscandian shield show that the temperatures of the investigated crustal level experienced a maximum of 50–70 °C during the time of calcite–pyrite precipitation[35,58]. These temperatures are much lower than those needed for TSR (>100 °C)[59], which can thus be ruled out as a pathway for pyrite formation. Taken together, the isotopic signatures detected, together with previously documented MSR-related pyrite $\delta^{34}S$ values from Olkiluoto, Finland[60], suggest widespread ancient MSR in the deep fracture networks of the Fennoscandian shield.

Molecular evidence for deep ancient life. The UCM detected in the solid bitumen extract of Kallmora #19334861 together with the absence of *n*-alkanes in that material (Supplementary Fig. 5) is a typical sign of biodegradation[41,61] and therefore provides further evidence for microbial utilization in situ of the primary expelled hydrocarbons of proposed shale origin. In addition, methyl-branched (*i*-$C_{17:0}$, *ai*-$C_{17:0}$, and *i*-$C_{18:0}$) and straight-chained (especially $C_{16:0}$, $C_{17:0}$, and $C_{18:0}$) fatty acids were preserved within the calcite coating in paragenesis with pyrite (Fig. 5). $C_{16:0}$ and $C_{18:0}$ are common in many organisms, whereas $C_{17:0}$ and the methyl-branched fatty acids can be used as biomarkers for sulfate reducing bacteria (SRB)[62–64], especially in combination with their $\delta^{13}C$ signature. *ai*-$C_{17:0}$ and $C_{17:0}$ are depleted in ^{13}C compared to co-occurring solid bitumen by 9–11‰ (−41 and −39‰ vs. −30‰), which is in line with the stable carbon isotope fractionation during heterotrophic bacterial sulfate reduction (BSR)[63]. Heterotrophic BSR is further supported by the depleted $\delta^{13}C$ signal of the coeval calcite (Fig. 2). SRB biomarkers are less abundant in Kallmora #18921093 (Supplementary Fig. 6), which only includes the methanogenesis-related $\delta^{13}C_{calcite}$ values. It is therefore underlined that BSR caused the superheavy $\delta^{34}S$ values in pyrites of Kallmora #19334681. This secondary biogenicity evidence is crucial, as there have been reports from the sedimentary record that superheavy pyrite may form also from TSR[65].

Morphological evidence for deep ancient life. As most of the samples are not newly retrieved from the mines, focus is on completely mineralized morphological remains of microbial communities, interpreted as indigenous. The remnants of completely mineralized interconnected networks of filamentous structures with anastomosing and branching filaments occurring in spatial relation to bitumen in a sample from Lund (Fig. 6c–e) resemble in morphology, size, mineralization, and occurrence of previously described endolithic fungal fossils reported from both the Fennoscandian shield[31,66] and from the ocean floor[67]. Desiccation of biofilms can sometimes result in patterns of interconnected ridges with filamentous-like appearances. However, these desiccation features are the result of biofilm contraction with non-circular ridges of highly variable diameters and with a topped morphology. In contrast, the described microstructures are distinct filaments with circular and even diameters throughout their lengths (Fig. 6c), and hence in favor of a microbial interpretation over an abiotic explanation. Without supporting organic data or biomarkers such as chitin, it is difficult to assign a certain biological affinity to the purported filaments. However, the frequent anastomoses between branches (Fig. 6c, e) exclude a prokaryotic interpretation of the fossils and favors of a fungal interpretation[66,67]. The partly carbonaceous filamentous structures from Grängesberg (Fig. 6h) also correspond in size and occurrence to previously described chitin-bearing fungal hyphae from the Fennoscandian shield[31]. Similar, partly carbonaceous preservation has been seen in several fungal fossils previously[66]. Lack of further diagnostic morphology makes a final fungal conclusion frail, although the behavior of potential hyphae reaching between the bitumen spheres suggests a trophic exploration.

The longitudinal shape with coherent diameter and rounded tip of the corrosion structures suggest that they could be produced by microorganisms (Fig. 6f), in particular an organism with grazing behavior as the shape with a rounded tip could correspond to known morphology of fungal hyphae. However, a biological explanation cannot satisfactorily be supported based solely on the morphology.

A temporal shift in metabolisms. Spatially coupled analytical spots for stable isotopes and geochronology within zoned calcite–pyrite assemblages provide distinction of the shift from methanogenesis at ca. 50–30 Ma to sulfate reduction at 19–13 Ma. The onset of the methanogenesis stage may be related to far-field fracture reactivation during the Pyrenean-Alpine orogeny that led to infiltration of microbial communities with descending surficial waters, at temperatures and salinities that were more suitable for microbial colonization than the previous bitumen infiltration stages[21]. Similar Sr isotope composition of the ^{13}C-rich calcite samples in Bergslagen points to a regional infiltration event during the Cenozoic methanogenesis event. The Sr isotope values are, however, much higher than contemporaneous seawater values (0.7075–0.7090,[68]), which means that water–rock interaction along the fracture flow paths has a large control on the Sr isotope values of the deep fluids. This is in agreement with findings at the tunnel system Äspö, Sweden, where Baltic seawater infiltrated to several hundred meters deep rapidly inherits more radiogenic Sr compositions due to ion-exchange along the flow path[69]. Although methanogens and SRB can coexist, SRB usually successively outcompete methanogens for substrates as sulfate concentrations elevate[70]. The BSR stage is thus proposed to have occurred when a sulfate-rich water infiltrated the fracture system. At this stage, BSR exhausted the sulfate pool to a degree that led to precipitation of substantially ^{34}S-rich pyrite (Fig. 4). The BSR stage is temporally related to subsidence due to burial beneath Upper Cretaceous to Oligocene sediments, at least in the southern parts of Fennoscandia[58]. Fracture reactivation during an early Miocene uplift that affected the craton[58] may have introduced sulfate-rich basinal fluids to the deeper igneous fracture system and shifted the metabolisms to dominantly BSR. At Grängesberg, the shift from methanogenesis to BSR is associated

with a shift in $\delta^{18}O_{calcite}$ to higher values, which indicates a change in fluid origin and/or temperature (Supplementary Fig. 2), and at Kallmora, the outer calcite overgrowths have less radiogenic Sr isotopic composition, also in agreement with a new fluid infiltration event. Overall, the signs of microbial activity that are preserved in the mineral record seem to reflect separate episodic events. The U-Pb dating shows that the events that led to calcite precipitation can last for up to ~6–8 Myr (Figs. 2h and 3g, and Supplementary Fig. 3). The determined ages of microbial processes are >1.5 Gyr younger than the host rock, which suggests that the environmental conditions have only been favorable for subsurface life during late Phanerozoic in the Fennoscandian shield, in agreement with thermochronological data of the host rocks[35] and previous timing constraints of ancient microbial life in this shield, e.g., in the Siljan impact crater[21]. The determined ages are, however, from a time when land plants already had colonized the continents and can therefore not be used to test the hypothesis of whether life developed in the deep biosphere.

Omnipresence of biosignatures and their implications. The findings of pervasive ^{13}C-rich calcite confirm previous hypotheses of widespread long-term microbial methane formation in the vast environment that the igneous upper continental crust represents; however, these hypotheses were hitherto only based on biosignatures from two sites in Sweden[21,23] and on live communities of methanogens/methanotrophs from South Africa, Finland, Sweden, and Japan[10,11,13,14,70]. In particular, but not exclusively, the methanogenesis signatures are spatially related to seep oils and bitumen expelled from overlying sedimentary successions into the igneous basement fracture systems, to depths of almost 1 km. The widespread methanogenesis signatures are of particular interest, owing to that methane is a very potent greenhouse gas if released to the atmosphere[71,72]. Furthermore, ^{13}C-depleted calcite that is indicative for incorporation of C originating from microbial decomposition of organic matter, and potentially methane[73], occurs in nine additional mines.

For $\delta^{34}S_{pyrite}$, there is substantial variability and superheavy values at several of the investigated sites. A majority of the mines show $\delta^{34}S_{pyrite}$ values indicative for BSR, of which most feature superheavy $\delta^{34}S_{pyrite}$ values (i.e., >anticipated initial $\delta^{34}S_{SO4}$).

From the marine sedimentary record, superheavy pyrite has gained interest, as it may be a proxy for oxygen levels in the oceans and atmosphere, and more locally for the sulfate–methane transition zone[74]. Our results show, in similarity to findings from Laxemar and Forsmark[22], Sweden, no correlation between superheavy $\delta^{34}S_{pyrite}$ and AOM-related $\delta^{13}C_{calcite}$ values. Our nine new sites with superheavy pyrite determinations are in agreement with previously documented Swedish sites Laxemar ($\delta^{34}S_{pyrite}$: −54 to +132‰[22]), Forsmark (−42 to +67‰[22]), and Siljan (−42 to +78‰[21]), as well as Olkiluoto in Finland (−50 to +82‰[60]). Large $\delta^{34}S_{pyrite}$ variability, including superheavy values, thus appears to be a widespread biosignature for deep, ancient rock-hosted BSR in the Fennoscandian shield, a metabolic pathway also indicated by calcite-trapped fatty acid biomarkers and their compound-specific C isotope signatures (Fig. 5), relative to the potential substrate (bitumen).

It has been hypothesized that microbial activity in the continental igneous crust has been widespread during Earth's history[16,67], but direct evidence for this omnipresence is scarce. Our approach using a comprehensive set of subsurface mineral samples collected from 33 mines across the Fennoscandian shield reveals omnipresent biosignatures of deep ancient life across this craton, particularly in the central part where most the samples in this study are from. There are also isotopic signatures for MSR in pyrite from the eastern part of the Fennoscandian shield (Finland)[60]. Although no timing constraints have been presented for the Finnish biosignatures, they indicate that the eastern part of the shield has been colonized in similar manner as the investigated area of the current study. Taken together, the findings are complementary to previous scattered investigations of deep ancient and active microbial life from scientific boreholes and underground facilities on land[11–14,66,67,73], and suggest that life in the continental igneous crust is not an anomaly in time and space. This supports the idea of large-scale long-term microbial activity in the continental igneous crust[9,16,17]. It is, however, important to note that heating of organic-rich source rocks and migration of the expressed oils (bitumen) have been required to create many of the features documented in this study.

Furthermore, the findings show that diverse biosignatures of deep ancient microbial activity are preserved within mineral coatings over millions of years. Visualization of the time evolution in $\delta^{13}C$ and $\delta^{34}S$ enables to trace temporal shifts in dominating metabolisms. Preserved organic molecules and their compound-specific stable C isotope composition within mineral coatings provide a further line of evidence for biogenicity. Strategies for Mars exploration tackling life (ancient and recent) at depth have been suggested as favorable over search in surficial environments, mainly owing to high radiation that destroys organic remains of life rapidly[33]. The omnipresence of terrestrial biosignatures from deep ancient life in calcite and pyrite veins described in this study further emphasizes the importance of subsurface investigations in the search for extraterrestrial life.

Methods

Materials. A total of 49 mineral samples were examined from 33 open pit and underground mines from across the Fennoscandian shield (Fig. 1, including a few samples from quarries and excavations). The samples are dominantly from Paleoproterozoic host rocks, spanning from the Kiruna region in the north to southern Sweden, mainly from the Bergslagen mining area in central Sweden (Supplementary Fig. 1). This area holds numerous iron and base metal sulfide deposits occurring in volcanic ash interbedded with, e.g., marbles, and banded iron formations[75]. The succession of supracrustal rocks form inliers bound by plutonic rocks intruded at 1.9–1.8 Ga[76] and shear zones. Low-temperature euhedral druse mineral assemblages of clay minerals, pyrite, calcite, zeolites, and solid bitumen occur in late-stage cavities and veins of the reactivated ore and shear zones, and are the focus of the current study. The host rock of each mine is listed in Supplementary Data 1. Most of the mineral samples were originally collected during mining operations in deep mines that are no longer accessible. Therefore, they represent a unique widespread sample record of the subsurface fracture systems. Most of the sample specimens belong to the collections of the Swedish Museum of Natural History, Stockholm, Sweden, except for the samples from accessible underground mines at Garpenberg and Dannemora, which were courtesy collected and provided by mining geologists.

The mineralogy and appearance of the fracture coating specimens were examined using a Hitachi S-3400N scanning electron microscope (SEM) equipped with an integrated energy dispersive spectrometry (EDS) system and a environmental SEM with a FEI QUANTA FEG 650 (ThermoFisher Scienfitic, USA) fitted with an Oxford X-Max 80 mm^2 EDS detector (Oxford Instruments, UK). The analyses were performed in low vacuum to minimize surficial charging effects. This enables the use of uncoated samples and, thus, EDS analyses of the C content. The acceleration voltage was 20 or 15 kV depending on the nature of the sample and the instrument was calibrated with a cobalt standard. Peak and element analyses were done using INCA Suite 4.11 software and normalized to 100 wt%. Element mapping was done using Aztec software. The calcite and pyrite crystals were hand-picked under the microscope for stable isotope analysis and geochronology, and solid bitumen aggregates were hand-picked for biomarker analysis.

Secondary ion mass spectrometry. Calcite and pyrite crystals were mounted in epoxy, polished to expose cross-sections, and examined with SEM to trace zonation and impurities prior to SIMS analysis. SIMS analysis (10 µm lateral beam dimension, 1–2 µm depth dimension) of carbon and oxygen isotopes in calcite and sulfur isotopes in pyrite was performed on a CAMECA IMS1280 ion microprobe following the analytical settings and tuning reported previously[50] with some differences; O was measured on two Faraday cups (FCs) at mass resolution 2500, whereas C used an FC/electron multiplier (EM) combination, with mass resolution 2500 on the ^{12}C peak and 4000 on the ^{13}C peak to resolve it from $^{12}C^1H$. The magnetic field was locked at the beginning of the session using an nuclear magnetic resonance field sensor. Secondary ion signals for ^{32}S and ^{34}S were detected

simultaneously using two Faraday detectors with a common mass resolution of 4860 ($M/\Delta M$). Data were normalized for instrumental mass fractionation (IMF) using matrix-matched reference materials, which were mounted together with the sample mounts and analyzed after every sixth sample analysis. Analyses were performed in automated sequences, with each analysis comprising a 70 s pre-sputter to remove the gold coating over a rastered 15 × 15 µm area, centering of the secondary beam in the field aperture to correct for small variations in surface relief and data acquisition in sixteen 4 s integration cycles. Results are reported as ‰ $\delta^{13}C$ and $\delta^{18}O$ based on the Pee Dee Belemnite (V-PDB) and reference value, and pyrite results are reported as ‰ $\delta^{34}S$ based on the Canon Diablo Troilite (V-CDT) reference value. Data were normalized for IMF using matrix-matched reference materials mounted together with the sample mounts and analyzed after every sixth sample analysis. The calcite reference material S0161, from a granulite facies marble in the Adirondack Mountains, was kindly provided by R.A. Stern (University of Alberta). The values used for IMF correction were determined by conventional stable isotope MS at Stockholm University on ten separate pieces, yielding $\delta^{13}C = -0.22 \pm 0.11$‰ V-PDB (1 SD) and $\delta^{18}O = -5.62 \pm 0.11$‰ V-PDB (1 SD). Precision was $\delta^{18}O$: ±0.2–0.3‰ and $\delta^{13}C$: ±0.4–0.5‰. The pyrite reference material S0302A with a conventionally determined value of 0.0 ± 0.2‰[77] was used. Typical precision on a single $\delta^{34}S$ value, after propagating the within-run and external uncertainties from the reference material measurements was ±0.10‰ (1σ). Values of the reference material measurements are listed together with the samples in Supplementary Data 2 and 3. In total, 627 analyses were made in calcite for $\delta^{13}C$, 65 for $\delta^{18}O$, and 452 for $\delta^{34}S$. Analytical results of the reference material measurements analyzed along with the unknown are listed in Supplementary Data 2 (C, O) and 3 (S). Mineralogical identification of pyrite and calcite was performed via X-ray diffraction, prior to SIMS analysis (Supplementary Figs. 7 and 8).

Scanning ion image (SII) analysis of selected sulfide crystals from #18910078 and #19334861 was performed with the same CAMECA IMS1280 instrument, utilizing a 20 kV incident energy, critically focused Cs^+ primary beam rastered over an area of 140 × 140 µm, following ref. [22]. The primary beam current of 20 pA correspond to a spatial resolution of <1 µm. Secondary ions were processed through the dynamic transfer optical system, a secondary beam raster located before the entrance slit to the mass spectrometer that steers the secondary beam back onto the ion optical axis of the instrument, to preserve its ability to generate flat-topped peaks at high mass resolution. The ion image acquisition software then reconstructs a given count to the correct emission point within the primary rastered area. The mass spectrometer was operated in peak-hopping mode at a mass resolution of 4500, sufficient to resolve ^{33}S from $^{32}S^1H$, and the two species ^{33}S and ^{34}S were measured in an ion-counting EM with an electronically gated deadtime of 44 ns. For each image, 200 cycles were measured, each analysis taking ca. 44 min that included a 10 min pre-sputter over an area of 150 × 150 µm to remove the gold coating, centering of the secondary beam in the field aperture and optimization of the mass calibration. In SII mode, all species must be detected using an EM, which has an upper count rate limit of 1.5 MHz. Therefore, to maximize the count rate on the least abundant isotope without risking an overload of the EM by the most abundant isotope, the ratio $^{34}S/^{33}S$ (≈5.6) was chosen in preference to the conventional $^{34}S/^{32}S$ (≈22.6), with correction to $\delta^{34}S$ during processing assuming only mass-dependent fractionation. Raw ion images were processed using the Winimage2 software, using previously determined $\delta^{34}S$ values from spot analyses to normalize the images to true values. Line scans were generated in the Winimage2 software using a 5 µm square box. The typical uncertainty on $\delta^{34}S$ in the line scans was ~3‰ (1σ, compared to ±0.13‰ from the spot analysis).

Bulk sample S isotope analysis. Sulfur isotopes in pyrite samples ($n = 7$) were determined by MC-ICP-MS analysis at the Vegacenter, Swedish Museum of Natural History, Stockholm, Sweden. The samples were dissolved on a hotplate, following ref. [78]. For each sample, 0.2–6 mg was weighed and was transferred to 7 ml Perfluoroalkoxy alkane vials. A volume of 1.5 ml 8 M HNO_3 was added to the samples and a blank. The vials were placed open on a 70 °C hotplate for evaporation. Once dry, 0.75 ml concentrated HNO_3 and 0.5 ml 6 M HCl was added before evaporating the samples again using the same procedure. The residues were dissolved in 0.3 M HNO_3 depending on sample size. Sample aliquots for element separation, assumed to contain 100 µg S, were transferred to clean vials and diluted ten times with de-ionized water to obtain 0.03 M HNO_3. International Atomic Energy Agency (IAEA) standards (S-1, S-3, and S-4) were dissolved in 0.3 M HNO_3 in a microwave oven. Aliquots of these solutions, containing ~100 µg S, were transferred to clean vials. These were diluted ten times with de-ionized water to obtain 0.03 M HNO_3. A volume of 0.1 ml of seawater reference CIT#39 was evaporated on a 70 °C hotplate and dissolved in 6 ml 0.03 M HNO_3. Purification of the samples, standards, seawater reference, and blank was performed using anion exchange chromatography using AG 1-X8 anion resin (analytical grade, 200–400 mesh, chloride form, 1 mL), following the elution scheme as provided in Supplementary Data 9. Before use, the resin and columns were cleaned by sequentially adding two reservoir volumes of de-ionized water, 6 M HCl and 0.1 M HCl/0.3 M HF for six cycles. This was followed by adding two reservoir volumes of 6 M HCl and de-ionized water. The total procedural blank ranged from 0.9% to 3.4% with a mean value of 1.7%.

Sulfur isotope ratios of the solutions were determined using a Nu Plasma II MC-ICP-MS and an Aridus II for sample introduction. A resolving power of ~10 000 ($M/\Delta M_{0.05\text{-}0.95}$) was achieved using a 25 µm resolution slit, which separates the sulfur isotope peaks from their overlaying isobaric interferences and presents an interference-free plateau for precise measurements. We confirmed previous observations[79] that the addition of Na to the samples increases the measured sensitivity with a preferred ratio of 1.5 to 3 for Na^+/SO_4^-. The setup resulted in a sensitivity of ~6.5 V/p.p.m. for ^{28}S, for solutions measured at 1.3 p.p.m. sulfur and 2 p.p.m. sodium. The sample uptake rate was ~100 µL/min, which resulted in ~600 µL sample consumption per analysis. Fractionation correction was performed by standard-sample bracketing with the IAEA-S-1 standard ($\delta^{34}S = -0.30\%_{VCDT}$). An on-mass zero measurement was performed at the beginning of each run in pure 0.3 M HNO_3 to account for instrumental sulfur background. The measured background was in the range of 80–100 mV for ^{28}S, which accounts for ~1% of the sample intensity. Each sample was measured three times in a row, in two separate analytical sessions. Results are presented as ‰ $\delta^{34}S$ normalized to the V-CDT scale. For quality control, reference solutions IAEA-S-4 (Soufre de Lacq) and CIT#39 were run repeatedly and treated as unknowns. The resulting $\delta^{34}S_{V\text{-}CDT}$ of 16.37 ± 0.67‰ ($n = 19$) and 20.92 ± 0.94‰ ($n = 9$), respectively, overlap with their corresponding literature values (16.90 ± 0.24‰[80] and ocean water sulfide: 20.99‰[81]). All samples and standards plot on a mass-dependent fractionation line between $\delta^{34}S$ and $\delta^{33}S$ with a slope of 0.515 (Supplementary Data 4), which indicates that isobaric interferences are properly corrected for.

LA-MC-ICP-MS $^{87}Sr/^{86}Sr$. $^{87}Sr/^{86}Sr$ values ($n = 30$) of calcite were determined by LA-MC-ICP-MS analysis at the Vegacenter, Swedish Museum of Natural History, Stockholm, Sweden, using a Nu plasma (II) MC-ICP-MS and an ESI NWR193 ArF eximer laser ablation system. Ablation frequency was 15 Hz, spot size 80 µm, and fluence 2.7 J/cm^2, and the same crystal growth zones analyzed with SIMS for $\delta^{13}C$ were targeted. Washout time was 40 s and ablation time was 40 s. The $^{87}Sr/^{86}Sr$ analyses were normalized to an in-house brachiopod reference material "Eccnomiosa gerda" (linear drift and accuracy correction) using a value established by TIMS of 0.709181 (2 SD 0.000004[82]). A modern oyster shell from Western Australia was used as a secondary reference material and was analyzed at regular intervals together with the primary reference. The accuracy of these analyses was quantified by comparison to the modern seawater value for $^{87}Sr/^{86}Sr$ of 0.7091792 ± 0.0000021[83]. Values of the reference material measurements are listed in Supplementary Data 4.

X-ray diffraction. A representative number of pyrite and calcite crystals (10–15) were picked from selected samples, pulverized in an agate mortar, and placed on a background-free Si-metal sample holder, to validate the samples mineralogy. X-ray powder diffraction data were recorded in a PANalytical X'Pert[3] Powder diffractometer system (Cu$K\alpha$-radiation $\lambda = 1.5406$ Å) operated at 40 mA and 45 kV. The data were collected between 5 and 70 2θ° for 20 min with an X'celerator silicon-strip detector. Background determination, peak positions, and search and match operations were performed using HighScore Plus software(4.6) and were corrected against an external Si standard (National Institute of Standards and Technology, NIST 640b); the patterns were matched to reference patterns (pyrite: ICSD-98-000-0316, calcite: ICSD-98-005-3529).

Organic geochemical analysis. Solely ultrapure organic solvents (pre-distilled and tested with GC-MS) and heated glassware (550 °C for 4 h) was used during organic geochemical preparation. Calcite crystals were extracted with dichloromethane (DCM; 2×) and *n*-hexane (1×) via ultrasonication (15 min at 20 °C, respectively) to eliminate potential surface contaminants and bitumen relics. The crystals were then powdered with a glass rod (heat-cleaned using a micro-torch). Calcite powders were decalcified by adding an excess of trimethylchlorosilane (TMCS)/methanol (1/9; *v*/*v*) at 35 °C for 2 h and 20 °C for 12 h, including simultaneous derivatization of released lipids. The lipid fraction was recovered by mixing with *n*-hexane (3×). The *n*-hexane extract was dried in a sample concentrator under a gentle stream of N_2 at 40 °C and re-dissolved in 200 µL *N*,*O*-bis(trimethylsilyl)-trifluoroacetamide (BSTFA) for further derivatization at 80 °C for 2 h. BSTFA was removed via N_2 at 40 °C and 50 µL of *n*-hexane was added before analysis with GC-MS. Chemical and laboratory blanks, as well as a 37-component fatty acid methyl ester standard (Supelco®), were analyzed in parallel. Compounds were identified by comparison to the standard and a NIST spectral library.

The Kallmora sample #19334861 (organic compound mixture in 50 µL *n*-hexane) was afterwards separated via column chromatography into three fractions as follows: (i) hydrocarbons, (ii) fatty acid methyl esters, and (iii) the polar residue, to try to isolate compounds of unknown composition that eluted together with fatty acid methyl esters and, consequently, to allow compound-specific stable carbon isotope analysis of the fatty acid methyl esters with GC-C-IRMS. Therefore, a glass column was filled with a methanol-cleaned frit plus 0.7 g silica gel (pre-heated at 550 °C for 2 h) and conditioned with *n*-hexane. The liquid sample was vapor deposited on top of the column and (i) hydrocarbons were separated with 7 mL *n*-hexane, (ii) fatty acid methyl esters with 7 mL DCM, and (iii) the polar residue with 20 mL DCM/methanol (1/1; *v*/*v*). The fractions were dried (N_2 at 40 °

C) and re-dissolved in 10 µL *n*-hexane for GC-MS and fatty acid methyl esters were additionally analyzed via GC-C-IRMS.

Crushed solid bitumen from Kallmora was extracted with DCM/methanol (3/1; v/v; 1×) and DCM (2×) via ultrasonication (10 min at 20 °C, respectively). The total organic extract was concentrated (N_2 at 40 °C) and an excess of chilled *n*-pentane was added to precipitate asphaltenes. After centrifugation (30 min, 2000 r.p.m.) the clear *n*-pentane (maltene fraction) was recovered and desulfurized with reduced Cu overnight. The maltene fraction was dried (N_2 at 40 °C) and re-dissolved in 1 mL *n*-hexane before GC-MS analysis.

Molecular analysis was performed using a Thermo Trace 1310 GC coupled to a Thermo TSQ Quantum Ultra triple quadrupole MS (settings in ref. [84]). Compound-specific stable carbon isotope ratios of the fatty acid methyl ester fraction from Kallmora #19334861 were determined with a Thermo Trace GC coupled to a Delta Plus IRMS via a combustion reactor (settings in ref. [84]). Changes in $\delta^{13}C$ due to addition of a methyl group from methanol during TMCS/methanol derivatization were tracked by determining the $\delta^{13}C$ value of the methanol and corrected accordingly. Bulk $\delta^{13}C$ of the solid bitumen sample was measured on a Thermo Delta V Advantage MS connected with a Thermo Flash 2000 elemental analyzer.

LA-ICP-MS U-Pb. U-Pb geochronology via the in situ LA-ICP-MS method was conducted at the Geochronology & Tracers Facility, British Geological Survey (Nottingham, UK). The method utilizes a New Wave Research 193UC excimer laser ablation system, coupled to a Nu Instruments Attom single-collector sector-field ICP-MS. The method follows previously described methods[85] and involves a standard-sample bracketing with normalization to NIST 614 silicate glass[86] for Pb-Pb ratios and WC-1 carbonate[85] for U-Pb ratios. The laser parameters comprised a 80 µm static spot, fired at 10 Hz, with a ~5 J/cm^2 fluence, for 20 s of ablation. Material is pre-ablated to clean the sample site with 150 µm spots for 2 s. Ages are determined by regression and the lower intercept on a Tera-Wasserburg plot (using Isoplot 4.15). ASH15D[87] was used as a validation and pooling of all sessions yields a lower intercept age of 2.989 ± 0.066 Ma overlapping the published age of 2.965 Ma. All ages are plotted and quoted at 2σ and include propagation of systematic uncertainties according to the protocol described previously[88]. Data are screened for low Pb and low U counts below detection, and very large uncertainties on the Pb-Pb and Pb-U ratios, which indicate mixed analyses.

Three samples were dated using U-Pb geochronology. One sample provided a robust regression exhibiting a single age. The other two samples yielded variable lower intercept ages that correlated well with the zonation visible in the SEM imagery. In most cases, the data did not exhibit a wide spread in Pb/U ratios, precluding free regression in Tera-Wasserburg space. Thus, to obtain lower intercept ages, the data were anchored to an estimated common lead $^{207}Pb/^{206}Pb$ of 0.9 ± 0.1. This value was based on the free regression of two sample populations that yielded values of 0.877 and 0.977, and measurement of cogenetic pyrite in one sample that yielded a value of ca. 0.96. It should be noted that our choice of $^{207}Pb/^{206}Pb_c$ for anchoring has minimal effect on the final ages within the stated ranges and uncertainties in the text. Full analytical data from the sessions are listed in Supplementary Data (ages in 5, raw data in 6, and analytical conditions in 8).

Data availability

All relevant data are included in the Supplementary Material of this article and stored publically available in the archive at Swedish National Data Service (doris.snd.gu.se) and traceable via the article title.

Received: 20 January 2021; Accepted: 20 April 2021;
Published online: 03 June 2021

References

1. Pedersen, K. Exploration of deep intraterrestial microbial life: current perspectives. *FEMS Microbiol. Lett.* **185**, 9–16 (2000).
2. Hoehler, T. M. & Jorgensen, B. B. Microbial life under extreme energy limitation. *Nat. Rev. Microbiol.* **11**, 83–94 (2013).
3. McMahon, S. & Parnell, J. Weighing the deep continental biosphere. *FEMS Microbiol. Ecol.* **87**, 113–120 (2014).
4. Magnabosco, C. et al. The biomass and biodiversity of the continental subsurface. *Nat. Geosci.* https://doi.org/10.1038/s41561-018-0221-6 (2018).
5. Knittel, K. & Boetius, A. Anaerobic oxidation of methane: progress with an unknown process. *Annu. Rev. Microbiol.* **63**, 311–334 (2009).
6. Goodwin, A. M. in *Principles of Precambrian Geology* (ed. Goodwin, A. M.) 1–50 (Academic, 1996).
7. Gleeson, T., Befus, K. M., Jasechko, S., Luijendijk, E. & Cardenas, M. B. The global volume and distribution of modern groundwater. *Nat. Geosci.* **9**, 161–167, https://doi.org/10.1038/ngeo2590 (2016).
8. Drake, H., Tullborg, E.-L. & Mackenzie, A. B. Detecting the near-surface redox front in crystalline bedrock using fracture mineral distribution, geochemistry and U-series disequilibrium. *Appl. Geochem.* **24**, 1023–1039 (2009).
9. Pedersen, K. Microbial life in granitic rock. *FEMS Microbiol. Rev.* **20**, 399–414 (1997).
10. Simkus, D. N. et al. Variations in microbial carbon sources and cycling in the deep continental subsurface. *Geochim. Cosmochim. Acta* **173**, 264–283 (2016).
11. Bomberg, M., Nyyssönen, M., Pitkänen, P., Lehtinen, A. & Itävaara, M. Active microbial communities inhabit sulphate-methane interphase in deep bedrock fracture fluids in Olkiluoto, Finland. *Biomed. Res. Int.* **2015**, 979530 (2015).
12. Pedersen, K. et al. Numbers, biomass and cultivable diversity of microbial populations related to depth and borehole-specific conditions in groundwater from depths of 4 to 450 m in Olkiluoto, Finland. *ISME J.* **2**, 760–775 (2008).
13. Lau, M. C. Y. et al. An oligotrophic deep-subsurface community dependent on syntrophy is dominated by sulfur-driven autotrophic denitrifiers. *Proc. Natl Acad. Sci. USA* **113**, E7927–E7936 (2016).
14. Ino, K. et al. Ecological and genomic profiling of anaerobic methane-oxidizing archaea in a deep granitic environment. *ISME J.* https://doi.org/10.1038/ismej.2017.140 (2017).
15. Eme, L., Spang, A., Lombard, J., Stairs, C. W. & Ettema, T. J. G. Archaea and the origin of eukaryotes. *Nat. Rev. Microbiol.* **15**, 711–723 (2017).
16. McMahon, S. & Parnell, J. The deep history of Earth's biomass. *J. Geol. Soc.* **175**, 716 (2018).
17. Pedersen, K. et al. Evidence of ancient life at 207 m depth in a granitic aquifer. *Geology* **25**, 827–830 (1997).
18. Tillberg, M. et al. Re-evaluating the age of deep biosphere fossils in the Lockne impact structure. *Geosciences* **9**, https://doi.org/10.3390/geosciences9050202 (2019).
19. Ivarsson, M. et al. Fungal colonization of an Ordovician impact-induced hydrothermal system. *Sci. Rep.* **3**, 3487 (2013).
20. Heim, C. et al. Ancient microbial activity recorded in fracture fillings from granitic rocks (Äspö Hard Rock Laboratory, Sweden). *Geobiology* **10**, 280–297 (2012).
21. Drake, H. et al. Timing and origin of natural gas accumulation in the Siljan impact structure, Sweden. *Nat. Commun.* **10**, 4736 (2019).
22. Drake, H. et al. Unprecedented 34S-enrichment of pyrite formed following microbial sulfate reduction in fractured crystalline rocks. *Geobiology* **16**, 556–574 (2018).
23. Drake, H. et al. Isotopic evidence for microbial production and consumption of methane in the upper continental crust throughout the Phanerozoic eon. *Earth Planet. Sci. Lett.* **470**, 108–118 (2017).
24. Bengtson, S. et al. Fungus-like mycelial fossils in 2.4-billion-year-old vesicular basalt. *Nat. Ecol. Evol.* **1**, 0141 (2017).
25. McKinley, J. P., Stevens, T. O. & Westall, F. Microfossils and paleoenvironments in deep subsurface basalt samples. *Geomicrobiol. J.* **17**, 43–54 (2000).
26. Sakakibara, M., Sugawara, H., Tsuji, T. & Ikehara, M. Filamentous microbial fossil from low-grade metamorphosed basalt in northern Chichibu belt, central Shikoku, Japan. *Planet. Space Sci.* **95**, 84–93 (2014).
27. Reitner, J., Schumann, G. & Pedersen, K. in *Fungi in Biogeochemical Cycles* (Cambridge Univ. Press, 2006).
28. Bengtson, S. et al. Deep-biosphere consortium of fungi and prokaryotes in Eocene subseafloor basalts. *Geobiology* **12**, 489–496 (2014).
29. Ivarsson, M. et al. Zygomycetes in vesicular basanites from Vesteris Seamount, Greenland Basin – a new type of cryptoendolithic fungi. *PLoS ONE* **10**, e0133368 (2015).
30. Klein, F. et al. Fluid mixing and the deep biosphere of a fossil Lost City-type hydrothermal system at the Iberia Margin. *Proc. Natl Acad. Sci. USA* **112**, 12036 (2015).
31. Drake, H. et al. Fossilized anaerobic and possibly methanogenesis-fueling fungi identified deep within the Siljan impact structure, Sweden. *Commun. Earth Environ.* **2**, 34 (2021).
32. Curiale, J. A. Origin of solid bitumens, with emphasis on biological marker results. *Org. Geochem.* **10**, 559–580 (1986).
33. Onstott, T. C. et al. Paleo-rock-hosted life on Earth and the search on Mars: a review and strategy for exploration. *Astrobiology* **19**, 1230–1262 (2019).
34. Drake, H., Ivarsson, M., Tillberg, M., Whitehouse, M. & Kooijman, E. Ancient microbial activity in deep hydraulically conductive fracture zones within the Forsmark target area for geological nuclear waste disposal, Sweden. *Geosciences* **8**, https://doi.org/10.3390/geosciences8060211 (2018).
35. Guenthner, W. R., Reiners, P. W., Drake, H. & Tillberg, M. Zircon, titanite, and apatite (U-Th)/He ages and age-eU correlations from the Fennoscandian Shield, southern Sweden. *Tectonics* **36**, 1254–1274 (2017).
36. Sandström, B., Tullborg, E.-L., de Torres, T. & Ortiz, J. E. The occurrence and potential origin of asphaltite in bedrock fractures, Forsmark, central Sweden. *GFF* **128**, 234–242 (2006).

37. Welin, E. The occurrence of asphaltite and thucholite in the Precambrian bedrock of Sweden. *Geologiska Föreningen i Stockholm Förhandlingar* **87**, 509–526 (1966).
38. Ahmed, M., Lehnert, O., Fuentes, D. & Meinhold, G. Origin of oil and bitumen in the Late Devonian Siljan impact structure, central Sweden. *Org. Geochem.* **68**, 13–26 (2014).
39. Milkov, A. V. in *Hydrocarbons, Oils and Lipids: Diversity, Origin, Chemistry and Fate* (ed. Wilkes, H.) 613–622 (Springer, 2020).
40. Milkov, A. V. & Etiope, G. Revised genetic diagrams for natural gases based on a global dataset of >20,000 samples. *Org. Geochem.* **125**, 109–120 (2018).
41. Head, I. M., Jones, D. M. & Larter, S. R. Biological activity in the deep subsurface and the origin of heavy oil. *Nature* **426**, 344–352 (2003).
42. Su, X., Zhao, W. & Xia, D. The diversity of hydrogen-producing bacteria and methanogens within an in situ coal seam. *Biotechnol. Biofuels* **11**, 245 (2018).
43. Pallasser, R. J. Recognising biodegradation in gas/oil accumulations through the $\delta^{13}C$ compositions of gas components. *Org. Geochem.* **31**, 1363–1373 (2000).
44. Parnell, J., Baba, M. U., Bowden, S. & Muirhead, D. Subsurface biodegradation of crude oil in a fractured basement reservoir, Shropshire, UK. *J. Geol. Soc.* (2017).
45. Meister, P. & Reyes, C. The carbon-isotope record of the sub-seafloor biosphere. *Geosciences* **9**, https://doi.org/10.3390/geosciences9120507 (2019).
46. Kim, S.-T. & O'Neil, J. R. Equilibrium and nonequilibrium oxygen isotope effects in synthetic carbonates. *Geochim. Cosmochim. Acta* **61**, 3461–3475 (1997).
47. Goodfellow, B. W., Viola, G., Bingen, B., Nuriel, P. & Kylander-Clark, A. R. C. Palaeocene faulting in SE Sweden from U-Pb dating of slickenfibre calcite. *Terra Nova* **29**, 321–328 (2017).
48. Böttcher, M. E., Smock, A. M. & Cypionka, H. Sulfur isotope fractionation during experimental precipitation of iron(II) and manganese(II) sulfide at room temperature. *Chem. Geol.* **146**, 127–134 (1998).
49. Kohn, M. J., Riciputi, L. R., Stakes, D. & Orange, D. L. Sulfur isotope variability in biogenic pyrite; reflections of heterogeneous bacterial colonization? *Am. Mineral.* **83**, 1454–1468 (1998).
50. Drake, H., Åström, M., Tullborg, E.-L., Whitehouse, M. J. & Fallick, A. E. Variability of sulphur isotope ratios in pyrite and dissolved sulphate in granitoid fractures down to 1 km depth - evidence for widespread activity of sulphur reducing bacteria. *Geochim. Cosmochim. Acta* **102**, 143–161 (2013).
51. Sim, M. S., Bosak, T. & Ono, S. Large sulfur isotope fractionation does not require disproportionation. *Science* **333**, 74–77 (2011).
52. Canfield, D. E. Isotope fractionation by natural populations of sulfate-reducing bacteria. *Geochim. Cosmochim. Acta* **65**, 1117–1124 (2001).
53. Kiyosu, Y. & Krouse, H. R. The role of organic acid in the abiogenic reduction of sulfate and the sulfur isotope effect. *Geochem. J.* **24**, 21–27 (1990).
54. King, H. E. et al. Sulfur isotope analysis of bitumen and pyrite associated with thermal sulfate reduction in reservoir carbonates at the Big Piney–La Barge production complex. *Geochim. Cosmochim. Acta* **134**, 210–220 (2014).
55. Li, P., Zou, H., Hao, F. & Yu, X. Sulfate sources of thermal sulfate reduction (TSR) in the Permian Changxing and Triassic Feixianguan formations, Northeastern Sichuan Basin, China. *Geofluids* **2019**, 5898901 (2019).
56. Ohmoto, H. & Goldhaber, M. B. in *Geochemistry of Hydrothermal Ore Deposits* (ed. Barnes, H. L.) 517–612 (Wiley, 1997).
57. Seal, R. R. II Sulfur isotope geochemistry of sulfide minerals. *Rev. Mineral. Geochem.* **61**, 633–677 (2006).
58. Japsen, P., Green, P. F., Bonow, J. M. & Erlström, M. Episodic burial and exhumation of the southern Baltic Shield: epeirogenic uplifts during and after break-up of Pangaea. *Gondw. Res.* **35**, 357–377 (2016).
59. Machel, H. G. Bacterial and thermochemical sulfate reduction in diagenetic settings - old and new insights. *Sediment. Geol.* **140**, 143–175 (2001).
60. Sahlstedt, E., Karhu, J. A., Pitkänen, P. & Whitehouse, M. Implications of sulfur isotope fractionation in fracture-filling sulfides in crystalline bedrock, Olkiluoto, Finland. *Appl. Geochem.* **32**, 52–69 (2013).
61. Philp, R. P. in *Hydrocarbons, Oils and Lipids: Diversity, Origin, Chemistry and Fate* (ed. Wilkes, H.) 1–42 (Springer, 2020).
62. Vainshtein, M., Hippe, H. & Kroppenstedt, R. M. Cellular fatty acid composition of Desulfovibrio species and its use in classification of sulfate-reducing bacteria. *Syst. Appl. Microbiol.* **15**, 554–566 (1992).
63. Londry, K. L., Jahnke, L. L. & Des Marais, D. J. Stable carbon isotope ratios of lipid biomarkers of sulfate-reducing bacteria. *Appl. Environ. Microbiol.* **70**, 745–751 (2004).
64. Hagenauer, A., Hippe, H. & Rainey, F. A. *Desulfotomaculum aeronauticum* sp. nov., a sporeforming, thiosulfate-reducing bacterium from corroded aluminium alloy in an aircraft. *Syst. Appl. Microbiol.* **20**, 65–71 (1997).
65. Cui, H. et al. Questioning the biogenicity of Neoproterozoic superheavy pyrite by SIMS. *Am. Mineral.* **103**, 1362–1400 (2018).
66. Drake, H. et al. Anaerobic consortia of fungi and sulfate reducing bacteria in deep granite fractures. *Nat. Commun.* **8**, 55 (2017).
67. Ivarsson, M. et al. The fossil record of igneous rock. *Earth Sci. Rev.* **210**, 103342 (2020).
68. Veizer, J. et al. $^{87}Sr/^{86}Sr$, $\delta^{13}C$ and $\delta^{18}O$ evolution of Phanerozoic seawater. *Chem. Geol.* **161**, 59–88 (1999).
69. Drake, H., Kooijman, E. & Kielman-Schmitt, M. Using $^{87}Sr/^{86}Sr$ LA-MC-ICP-MS transects within modern and ancient calcite crystals to determine fluid flow events in deep granite fractures. *Geosciences* **10**, https://doi.org/10.3390/geosciences10090345 (2020).
70. Ma, T.-T. et al. Coexistence and competition of sulfate-reducing and methanogenic populations in an anaerobic hexadecane-degrading culture. *Biotechnol. Biofuels* **10**, 207 (2017).
71. Hallbeck, L. & Pedersen, K. Culture-dependent comparison of microbial diversity in deep granitic groundwater from two sites considered for a Swedish final repository of spent nuclear fuel. *FEMS Microbiol. Ecol.* **81**, 66–77 (2012).
72. Hmiel, B. et al. Preindustrial 14CH4 indicates greater anthropogenic fossil CH4 emissions. *Nature* **578**, 409–412 (2020).
73. Drake, H. et al. Extreme ^{13}C-depletion of carbonates formed during oxidation of biogenic methane in fractured granite. *Nat. Commun.* **6**, 7020 (2015).
74. Borowski, W. S., Rodriguez, N. M., Paull, C. K. & Ussler Iii, W. Are ^{34}S-enriched authigenic sulfide minerals a proxy for elevated methane flux and gas hydrates in the geologic record? *Marine Petrol. Geol.* **43**, 381–395 (2013).
75. Allen, R. L., Lundstrom, I., Ripa, M. & Christofferson, H. Facies analysis of a 1.9 Ga, continental margin, back-arc, felsic caldera province with diverse Zn-Pb-Ag-(Cu-Au) sulfide and Fe oxide deposits, Bergslagen region, Sweden. *Econ. Geol.* **91**, 979–1008 (1996).
76. Stephens, M. B. et al. Synthesis of the bedrock geology in the Bergslagen region, Fennoscandian Shield, south-central Sweden. *Geol. Survey Sweden* **Ba 58**, 259 (2009).
77. Liseroudi, M. H. et al. Microbial and thermochemical controlled sulfur cycle in the Early Triassic sediments of the Western Canadian Sedimentary Basin. *J. Geol. Soc.* https://doi.org/10.1144/jgs2020-175 (2021).
78. Craddock, P. R., Rouxel, O. J., Ball, L. A. & Bach, W. Sulfur isotope measurement of sulfate and sulfide by high-resolution MC-ICP-MS. *Chem. Geol.* **253**, 102–113 (2008).
79. Paris, G., Sessions, A. L., Subhas, A. V. & Adkins, J. F. MC-ICP-MS measurement of $\delta^{34}S$ and $\Delta^{33}S$ in small amounts of dissolved sulfate. *Chem. Geol.* **345**, 50–61 (2013).
80. Qi, H. P. & Coplen, T. B. Evaluation of the $^{34}S/^{32}S$ ratio of Soufre de Lacq elemental sulfur isotopic reference material by continuous flow isotope-ratio mass spectrometry. *Chem. Geol.* **199**, 183–187 (2003).
81. Rees, C. E., Jenkins, W. J. & Monster, J. The sulphur isotopic composition of ocean water sulphate. *Geochim. Cosmochim. Acta* **42**, 377–381 (1978).
82. Kiel, S. et al. The paleoecology, habitats, and stratigraphic range of the enigmatic cretaceous Brachiopod Peregrinella. *PLoS ONE* **9**, e109260 (2014).
83. Mokadem, F. et al. High-precision radiogenic strontium isotope measurements of the modern and glacial ocean: Limits on glacial–interglacial variations in continental weathering. *Earth Planet. Sci. Lett.* **415**, 111–120 (2015).
84. Reinhardt, M. et al. Organic signatures in Pleistocene cherts from Lake Magadi (Kenya) – implications for early Earth hydrothermal deposits. *Biogeosciences* **16**, 2443–2465 (2019).
85. Roberts, N. M. W. et al. A calcite reference material for LA-ICP-MS U-Pb geochronology. *Geochem. Geophys. Geosyst.* **18**, 2807–2814 (2017).
86. Woodhead, J. D. & Hergt, J. M. Strontium, Neodymium and lead isotope analyses of NIST glass certified reference materials: SRM 610, 612, 614. *Geostand. Newslett.* **25**, 261–266 (2001).
87. Nuriel, P. et al. The use of ASH-15 flowstone as a matrix-matched reference material for laser-ablation U-Pb geochronology of calcite. *Geochronology* **3**, 35–47 (2021).
88. Horstwood, M. S. A. et al. Community-derived standards for LA-ICP-MS U-(Th-)Pb geochronology – uncertainty propagation, age interpretation and data reporting. *Geostand. Geoanal. Res.* **40**, 311–332 (2016).

Acknowledgements

Swedish research council (contract 2017-05186 to H.D., 2017-04129 to M.I.) and Formas (contracts 2017-00766 and 2020-01577 to H.D. and M.W.) are thanked for financial support. Volker Thiel is thanked for providing laboratory access to Göttingen University, and Jens Dyckmans for bulk $\delta^{13}C$ of solid bitumen and compound-specific $\delta^{13}C$ analyses. Kerstin Lindén is thanked for sample preparation assistance, Heejin Jeon for SIMS assistance, Karin Wallner for laboratory assistance, and Katerina Rodiouchkina for method development of S isotope analysis. Thanks to Johan Olsson, Boliden Mineral AB, for providing samples from the active mine in Garpenberg, Stefan Hagenfeldt for providing a sample from Dannemora, Geological Survey of Sweden for permission to use maps (case number 2011:1308), and to University of Gothenburg for access to SEM. This is NordSIM publication 678 and Vegacenter publication 039.

Author contributions

H.D. conceived the study. H.D. carried out SEM investigations, sample preparation, and microscopy of the mineral assemblages. H.D. and M.I. did microscopy and staining of filaments. N.M.W.R. carried out U-Pb carbonate geochronology. M.W. and H.D. carried out SIMS analysis. M.R. carried out GC-MS investigations and extraction. A.K. carried out XRD. E.K. and M.K.-S. handled (LA)-MC-ICP-MS. H.D. wrote the initial draft and N.M.W.R., M.R., and M.I. provided constructive edits to the text.

Funding

Open access funding provided by Linnaeus University.

Competing interests

The authors declare no competing interests.

Additional information

Supplementary information The online version contains supplementary material available at https://doi.org/10.1038/s43247-021-00170-2.

Correspondence and requests for materials should be addressed to H.D.

Peer review information Primary handling editor: Clare Davis.